Excited-State Intramolecular Hydrogen Transfer of Compact Molecules Controls Amyloid Aggregation Profiles

Mannkyu Hong,[†,‡,∥] Mingeun Kim,[†,∥] Jiwon Yoon,[§] Seung-Hee Lee,*[,§] Mu-Hyun Baik,*[,†,‡] and Mi Hee Lim*[,†]

[†]Department of Chemistry, Korea Advanced Institute of Science and Technology (KAIST), Daejeon 34141, Republic of Korea
[‡]Center for Catalytic Hydrocarbon Functionalizations, Institute for Basic Science (IBS), Daejeon 34141, Republic of Korea
[§]Department of Biological Sciences, Korea Advanced Institute of Science and Technology (KAIST), Daejeon 34141, Republic of Korea

*To whom correspondence should be addressed: miheelim@kaist.ac.kr, mbaik2805@kaist.ac.kr, and shlee1@kaist.ac.kr

[∥]These authors contributed equally to this work.

ABSTRACT

Designing new chromophores by tuning their molecular structures and optimizing their photophysical properties leads to suitable photochromic features. Herein, we report a series of **anthraquinone** (**AQ**)-based photosensitizers that undergoes excited-state intramolecular hydrogen transfer and effectively oxidizes amyloidogenic peptides, which significantly affects the subsequent aggregation pathways. DFT calculations showed that the appropriate position of the hydroxyl groups in the **AQ** backbone and the consequent intramolecular hydrogen transfer can facilitate the energy transfer to triplet oxygen. Biochemical and biophysical investigations confirmed that these photoactive chemical reagents are able to oxidatively modify both metal-free amyloid-β (Aβ) and metal-bound Aβ, thereby redirecting their on-pathway aggregation into off-pathway as well as disassembling their pre-formed aggregates. Moreover, the in vivo histochemical analysis of Aβ species produced upon photoactivation of the most promising candidate demonstrated that they do not aggregate into toxic oligomeric or fibrillar aggregates in the brain. Overall, our combined computational and experimental studies validate a light-based approach for designing small molecules as chemical reagents targeting and controlling amyloidogenic peptides associated with neurodegenerative disorders.

INTRODUCTION

Numerous chemical reagents were developed for photodynamic therapy (PDT) since the ground breaking discovery that eosin can be used to treat skin tumors.[1-7] Commercialized drugs, such as porfimer sodium (Photofrin), 5-aminolevulinic acid (ALA), methyl aminolevulinate (MAL), and methyl aminooxopenoat (MAOP), demonstrated the power of using light to target internal and skin tumors.[8-10] In general, PDT relies upon generating reactive oxygen species (ROS) upon photoactivation that can damage lipids, proteins, and nucleic acids, eventually triggering cell death or protein inactivation.[1,11,12] Recently, ROS-induced oxidative modifications of amyloid-β (Aβ) peptides have been recognized as an effective method for controlling their aggregation pathways that are directly linked to the pathology of Alzheimer's disease (AD).[13] Oxidation of Aβ peptides with photosensitizers[14] or redox-active molecules[15-20] may alter their abnormal assembly and improve cognitive defects in AD transgenic mice. A variety of photosensitizers ranging from fullerene[21] or porphyrin-based[22] macromolecules, organometallic complexes,[23-28] nanoparticles,[29,30] and organic molecules[31-34] were designed to modulate the aggregation of Aβ. Despite their remarkable potential, the complexity of synthesis, low permeability of the blood-brain barrier (BBB),[35,36] and the potential risk in toxicity37-39 remain significant hurdles to overcome.

We questioned if small organic photosensitizers carrying simple functionalities such as hydroxyl and carboxyl groups can oxidatively modify both metal-free Aβ and metal-bound Aβ (metal–Aβ) and alter their aggregation profiles. As shown in Figure 1a, we rationally selected a series of **anthraquinone** (**AQ**)-based compounds and tested their capacity to oxidize metal-free Aβ and metal–Aβ upon photoirradiation and, consequently, vary their aggregation. In addition, the detailed mechanism for such reactivity was determined. Moreover, the aggregation behaviors of Aβ species produced upon light activation of the most promising molecule were probed in vivo. Collectively, our studies demonstrate that compact molecules with proper structural and photophysical features can be developed for manipulating Aβ aggregation with light.

RESULTS AND DISCUSSION

AQ-based dyes have been used as photosensitizers for various applications such as photovoltaics,[40] photocatalysts,[41-43] photoactive peptides,[44] and cell imaging;[45] thus, we chose the **AQ** backbone to identify effective photosensitizers that can oxidatively modify Aβ peptides. As displayed in Figure 1a, a series of **AQ**-based molecules with simple structural variations composed of only three basic carbon, hydrogen, and oxygen atoms was selected for this work. Based on the parent structure **9,10-AQ**, the hydroxyanthraquinone derivatives were classified into
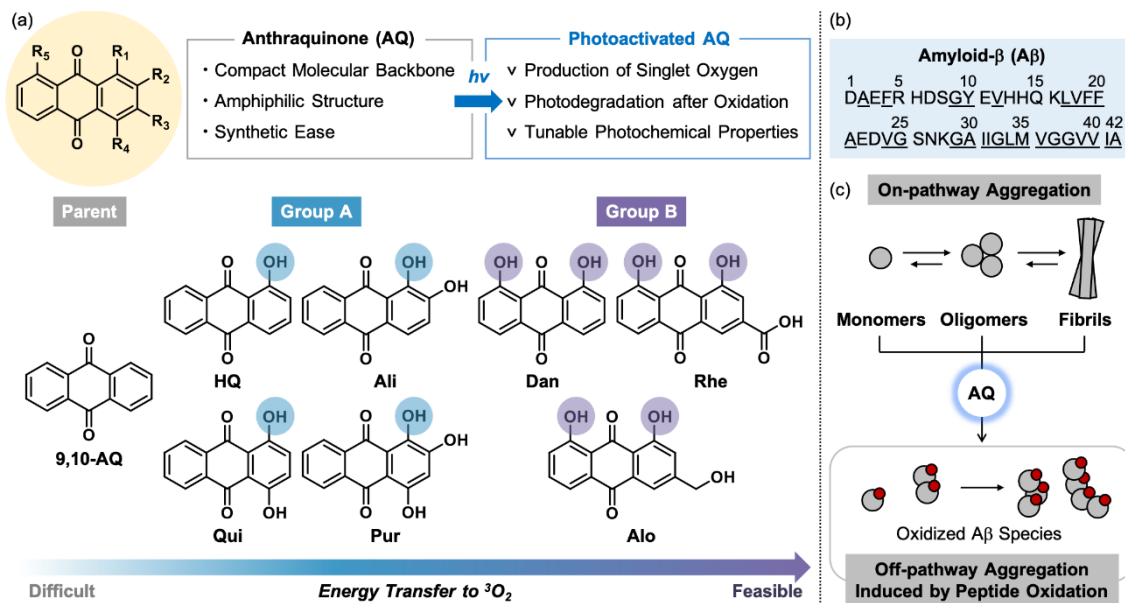
Figure 1. Rational selection of compact molecules that can modify the aggregation of Aβ with photoactivation. (a) Chemical structures and properties of **9,10-AQ** (**Parent**); **HQ**, **Ali**, **Qui**, **Pur** (**Group A**); **Dan**, **Rhe**, **Alo** (**Group B**). **9,10-AQ**, 9,10-anthraquinone; **HQ**, 1-hydroxyanthraquinone; **Ali** (alizarin), 1,2-dihydroxyanthraquinone; **Qui** (quinizarin), 1,4-dihydroxyanthraquinone; **Pur** (purpurin), 1,2,4-trihydroxyanthraquinone; **Dan** (dantron), 1,8-dihydroxyanthraquinone; **Rhe** (rhein), 4,5-dihydroxyanthraquinone-2-carboxylic acid; **Alo** (aloe-emodin), 1,8-dihydroxy-3-(hydroxymethyl)-anthraquinone. (b) Sequence of Aβ. Hydrophobic residues are underlined. (c) Schematic description of the on-pathway aggregation of Aβ with the modulatory strategy employing the photoactivated **AQ** series.

two groups: **Group A** (**HQ**, **Ali**, **Qui**, and **Pur**) possesses a hydroxyl group on the R_1 position forming one quasi-ring with the adjacent ketone and additional hydroxyl groups on R_2, R_4, or both; **Group B** (**Dan**, **Rhe**, and **Alo**) contains hydroxyl groups on both R_1 and R_5 generating two quasi-rings and structural variance on R_3. The anthraquinone skeleton and the aforementioned structural variation can offer several advantages in targeting Aβ. The **AQ** series has amphiphilic structures that can interact with Aβ consisting of both hydrophilic and hydrophobic amino acid residues, as visualized in Figure 1b. The addition of hydroxyl and carbonyl groups with the ketone functionality can provide additional binding sites with Aβ through hydrogen bonds. The anthracene π-plane backbone is not only essential for the photosensitizing ability but also enables hydrophobic interactions with the β-sheet in oligomeric and fibrillar Aβ.[46] Hydroxyl groups and the

neighboring ketone functionality are envisioned to serve as potential metal-binding sites that can interact with other metal ions bound to Aβ. Upon photoactivation, anthraquinones are reported to generate singlet oxygen ($^1O_2$), which are highly reactive towards diverse biological substrates.[47,48] As such, we anticipated that **AQ** derivatives could readily oxidize amino acid residues in Aβ. We evaluated $^1O_2$ production of compact molecules in the **AQ** series with mechanistic investigations and their reactivities towards both metal-free Aβ and metal–Aβ, as depicted in Figure 1c.

Mechanism for $^1O_2$ Generation. Density functional theory (DFT) calculations were performed to estimate the ability of our selected molecules to produce $^1O_2$ upon photoirradiation. As illustrated in Figure 2a, the energy transfer occurs from the triplet excited photosensitizer (^{3}**AQ**) to the acceptor triplet oxygen ($^3O_2$) resulting in a singlet ground state photosensitizer (^{1}**AQ**) and a singlet excited state acceptor ($^1O_2$).[49] Hydroxyanthraquinones exhibit excited-state intramolecular hydrogen transfer (ESIHT) from hydroxyl groups towards the adjacent ketone functionality during light activation.[50] Moreover, hydroxyanthraquinones with deuterium substituted hydroxyl groups are reported to have longer emission lifetimes compared to the non-substituted analogues.[51,52] Therefore, we can hypothesize that the energy transfer (i.e., donor relaxation) is directly linked to reverse intramolecular hydrogen transfer (RIHT). In support of this notion, the DFT-calculated barrier ($\Delta G^\ddagger$) of the energy transfer for **9,10-AQ** to produce $^1O_2$ is unrealistically high at 138.9 kcal/mol if intramolecular hydrogen transfer is not considered. The incorporation of the hydroxyl moiety enables intramolecular hydrogen transfer and reduces the triplet energy transfer barrier considerably, suggesting that hydroxyanthraquinones are suitable scaffolds for $^1O_2$ production. Specifically, calculations on **Group A** (**HQ**, **Ali**, **Qui**, and **Pur**; Figure 1a) that share a common backbone of 1-hydroxyl group next to the ketone functionality reveal low energy transfer barriers ranging from 1.3 up to 11.2 kcal/mol. The molecules in **Group B** (**Dan**, **Rhe**, and **Alo**) with 1- and 8-hydroxyl moieties are predicted to be most efficient and barrierless.

We questioned why the position of hydroxyl groups has such a dramatic impact on the energy transfer barriers towards $^3O_2$ excitation. The triplet energy transfer barrier can be divided in two principal components: thermodynamic driving force (ΔG) and reorganization energy (λ).[53-55] ΔG is the energy difference between the singlet-triplet energy gap of the donor and the acceptor. Comparing the frontier molecular orbitals of the donor scaffolds, all of our selected **AQ** derivatives bear delocalized singly occupied molecular orbital (SOMO) in their triplet state, as presented in Figure S1. The molecules in **Group A** present a smaller singlet-triplet energy gap of the donor where ΔG varies from –13.3 to 3.6 kcal/mol. This small energy gap is due to the biased position of electron-donating groups and the resulting localized highest occupied molecular orbital
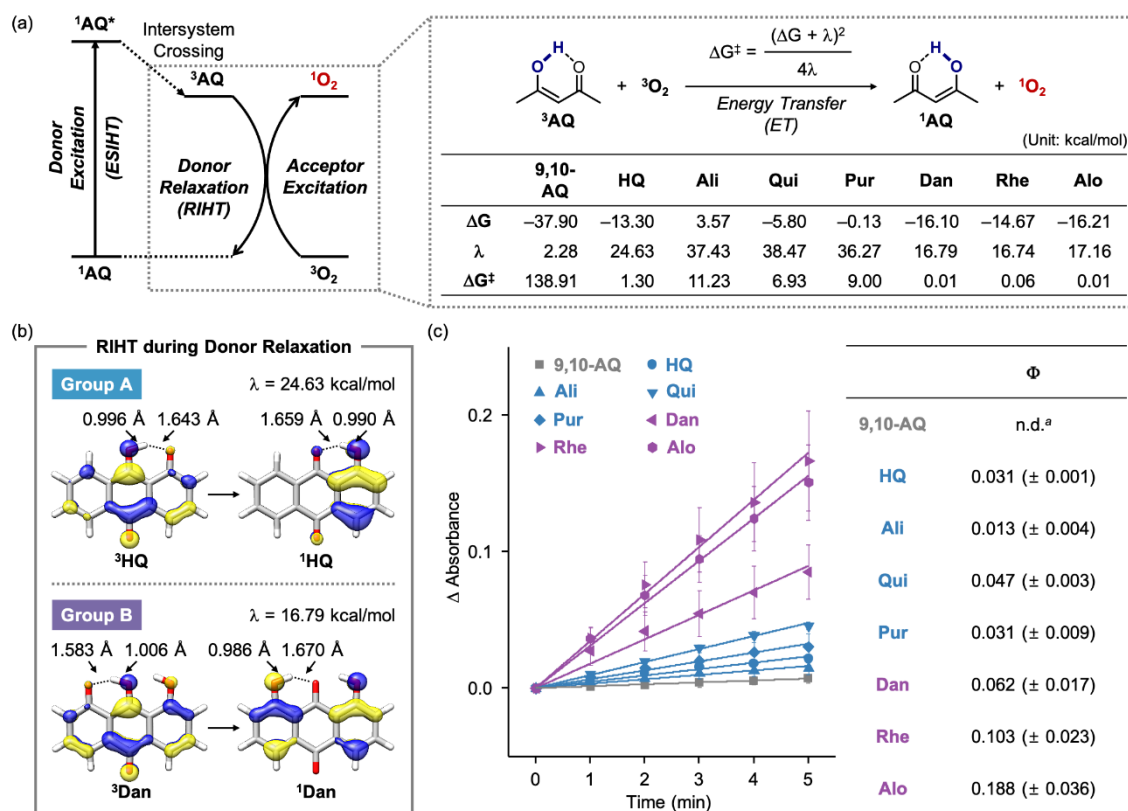
Figure 2. Production of $^1O_2$ by the **AQ** series upon photoactivation. (a) DFT-calculated energy transfer barriers ($\Delta G^{\ddagger}$) and their components (ΔG, singlet-triplet free energy gap; λ, reorganization energy) for each compound. (b) Structural comparison between **HQ** (**Group A**) and **Dan** (**Group B**) and the key intramolecular hydrogen transfer that determines the different reorganization energy. (c) Amount of $^1O_2$ generated by the **AQ** series with light exposure analyzed by the ABDA assay and their quantum yields (Φ). Error bars represent the standard error of the mean from three independent experiments. Conditions: [compound] = 25 µM; [ABDA] = 100 µM; room temperature; Kessil lamp (467 nm) for 0, 1, 2, 3, 4, and 5 min. [a]n.d., not determined due to the limited production of $^1O_2$.

(HOMO), which leads to a relatively unstable singlet ground state. The consequence is dramatic for the deprotonated **Ali** and **Pur** (ΔG of 3.6 kcal/mol and –0.1 kcal/mol, respectively) possessing phenolate moieties with a strong electron-donating character at neutral pH.[56] In contrast to **Group A**, the compounds in **Group B** retain symmetrically positioned hydroxyl groups with delocalized HOMO in the singlet ground state maintaining the singlet-triplet energy gap to a range of –16.2 to –14.7 kcal/mol.

Another factor in determining the barrier is λ associated with structural changes required for the energy transfer. Ranging from 24.6 to 38.4 kcal/mol, the molecules in **Group A** generally require higher λ values than those in **Group B** that show λ values of in the range of 16.7 to 17.1 kcal/mol. To better understand this trend, **HQ** (λ = 24.6 kcal/mol) and **Dan** (λ = 16.8 kcal/mol) were chosen to represent molecules in **Group A** and **Group B**, respectively, as depicted in Figure 2b. The hydrogen bond in ^{3}**HQ** shortens from 1.64 to 1.00 Å during donor relaxation, while the hydrogen bond involved in the hydrogen transfer in 3Dan displays a smaller change from 1.58 to 0.99 Å, indicating a reduced reorganization penalty compared to that of ^{3}**HQ**. Two explanations can be offered to unveil the role of the additional hydroxyl group at the R_1 position of **Dan**. In the context of intramolecular resonance-assisted hydrogen bonding, the extra hydroxyl functionality can serve as a π-electron-donating group to strengthen the hydrogen bond motif and, subsequently, shortens it.[57] As another aspect, the additional hydrogen bond donor can withdraw the electron density from the interacting hydroxyl group and lower its pK_a facilitating the hydrogen transfer process back to the singlet ground state structure. We reoptimized the triplet structure of ^{3}**Dan** with the supplementary hydroxyl group to face the opposite direction and observed a slight elongation of the hydrogen bond length to 1.61 Å, which validates the dual effect of the hydroxyl group at R_1 in **Group B**, as described in Figure S2.

An alternative mechanism can be proposed for the excitation and relaxation of the photosensitizers during the triplet energy transfer: the stepwise procedure where the vertical relaxation of the triplet state comes first and RIHT comes later, as shown in Figure S3. Note that the mechanism of the concerted or stepwise pathway is still under debate because of the undetectable phosphorescence for hydroxyanthraquinones. Two types of vertical relaxation were examined through DFT and time-dependent density functional theory (TD-DFT) calculations: the **AQ** series that (i) undergoes ESIHT in a stepwise manner or (ii) does not transfer their hydrogen upon excitation. In both of these cases, the reorganization energy is negligible and the singlet-triplet energy gap is the only factor that determines the triplet energy transfer. According to our calculations, the ESIHT-assisted models exhibit an adequate energy gap to facilitate the triplet energy process. **HQ**, **Ali**, **Qui**, and **Pur** have an energy gap ranging from 10.8 to 22.0 kcal/mol that is insufficient for converting $^3O_2$ to $^1O_2$, while the energy gap of **Dan**, **Rhe**, and **Alo** ranges from 21.6 to 23.2 kcal/mol comparable to the energy of 22.5 kcal/mol needed to activate inert $^3O_2$. On the other hand, our hypothetical model that does not go through ESIHT and directly to intersystem crossing yields a larger singlet-triplet energy gap. **HQ** has an energy gap of 42.6 kcal/mol, but **Ali** and **Pur** present an energy gap between 12.4 and 18.9 kcal/mol that is too small. **Dan**, **Rhe**, and **Alo** have energy gaps in the range of 40.6 to 43.4 kcal/mol, rendering them

incompetent to achieve effective triplet energy transfer to the oxygen acceptor. Therefore, ESIHT plays a significant role for the **AQ** series not only in the concerted but also in the stepwise mechanism to become appropriate photosensitizers by controlling the singlet-triplet energy gap. Taken together, our computational studies highlight the importance of additional hydroxyl groups and reveal that the position of hydrogen bond donors are key to facilitate the triplet energy transfer.

$^1O_2$ Production. Photochemical properties of the **AQ** series used in this study were examined by ultraviolet–visible (UV–Vis) and fluorescence spectroscopies. As summarized in Figure S4, the absorption spectra of the **AQ** series in dimethyl sulfoxide (DMSO) or the buffered solution showed maxima in the range of 326–486 and 335–516 nm, respectively, denoting photon absorbance in the blue light region. Especially, the absorption of **Ali** and **Pur** in the buffered solution displayed bathochromic shifts (λ = 82 and 21 nm, respectively), relative to maximum in DMSO, because the hydroxyl group at the R_2 position is deprotonated at neutral pH.[56] Moreover, the luminescence spectra of the **AQ** series in DMSO and the buffered solution were measured, as presented in Figure S5. While **9,10-AQ** had a maximum emission wavelength at 425 nm in DMSO and diminished absorbance in the buffered solution, the rest of the **AQ** series emitted light within the range of 554–612 nm upon illumination. Luminescence of **Ali** and **Pur** was not observed in the buffered solution.

The capability of the AQ series to produce 1O2 in the wavelength of the blue light spectrum (ca. 467 nm) was evaluated employing the ABDA assay [ABDA = 9,10-Anthracenediyl-bis(methylene)-dimalonic acid]. As illustrated in Figures 2c and S6, the absorbance attenuation (ΔA) of ABDA in the presence of the **AQ** series under aerobic conditions revealed the energy transfer from the compounds in **Group B** towards O_2 exhibiting a range of Φ from 0.062 up to 0.188 comparable to $[Ru(bpy)_3]^{2+}$ (Φ = 0.18 in H_2O)[58-60] as a reference molecule. The molecules in **Group A** displayed moderate or low $^1O_2$ formation with a Φ range from 0.013 to 0.047. Note that the Φ value of **9,10-AQ** could not be obtained due to the minimum changes of the absorption peaks of ABDA. Therefore, the photochemical measurements confirm that the **AQ** series generates $^1O_2$ and the molecules in **Group B** are most effective. These results are in line with the computational estimates of the triplet energy transfer barrier.

Aβ Oxidation. To determine whether the **AQ** series can oxidatively modify metal-free and metal–Aβ with photoirradiation under aerobic conditions, the resultant Aβ species were analyzed by electrospray ionization–mass spectrometry (ESI–MS) and tandem MS (ESI–MS^2). As displayed in Figure 3, no significant change in metal-free Aβ$_{40}$ was observed in the absence of light. Upon
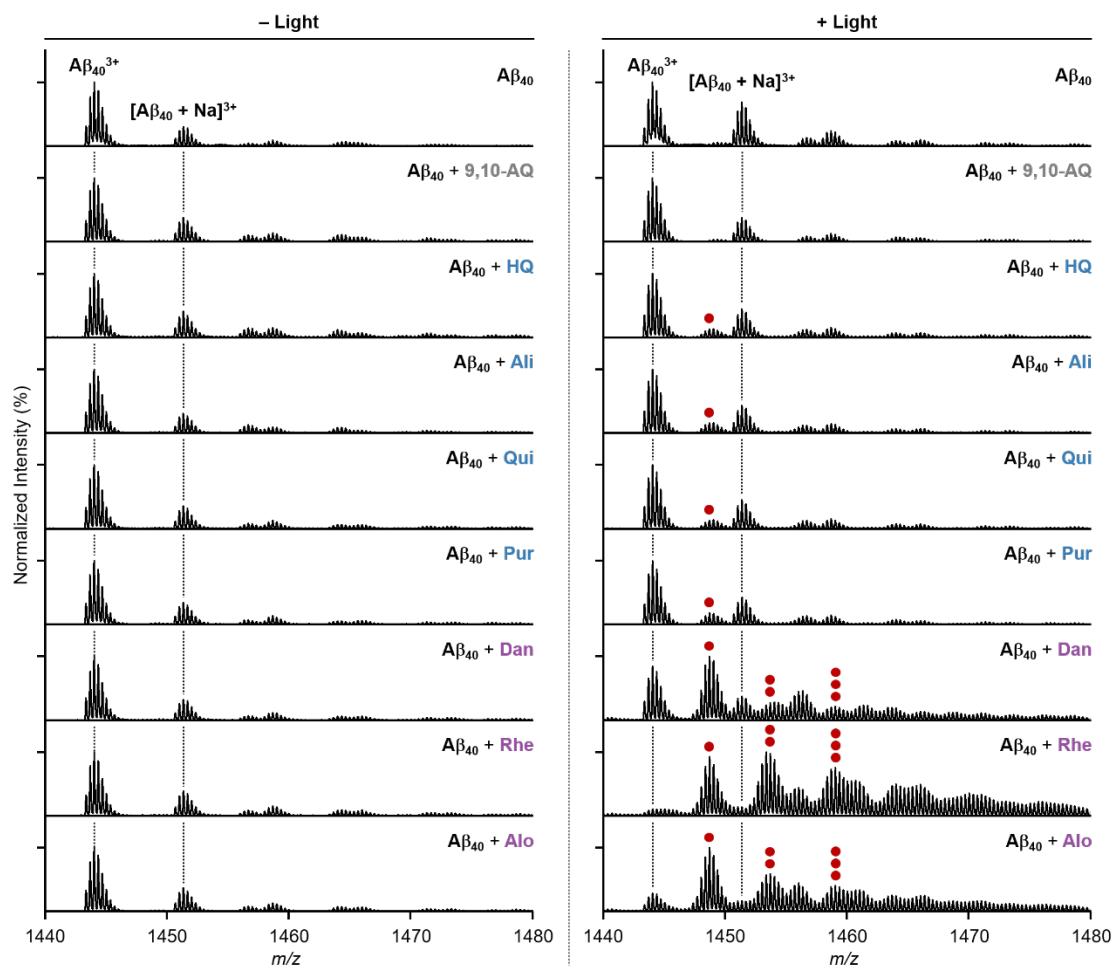
Figure 3. Analysis of $A\beta_{40}$ species produced by treatment of the **AQ** series with and without light exposure by ESI–MS. The number of red dots represents the number of oxygen atoms incorporated into $A\beta_{40}$ monomer $[A\beta_{40} + nO]^{3+}$ (n = 1, 2, or 3). Conditions: $[A\beta_{40}]$ = 25 μM; [compound] = 50 μM; 20 mM ammonium acetate (1% v/v DMSO), pH 7.4; 37 °C; 3 h; constant agitation (250 rpm); Kessil lamp (467 nm) for 1 h. The samples were diluted by 5-fold with H_2O before injection to the mass spectrometer.

photoactivation of the **AQ** series, the peaks corresponding to oxidized $A\beta_{40}$ species were monitored. The parent molecule **9,10-AQ** did not affect $A\beta_{40}$ despite light exposure. When **HQ**, **Ali**, **Qui**, and **Pur** (**Group A**) were exposed to $A\beta_{40}$, a new peak was detected at 1,448 *m/z*, indicative of the incorporation of a single oxygen atom into monomeric $A\beta_{40}$. In the case of **Dan**, **Rhe**, and **Alo** (**Group B**), three new peaks were detected at 1,448, 1,453, and 1,459 *m/z* corresponding to the singly, doubly, and triply oxidized $A\beta_{40}$ monomers, respectively. The singly,
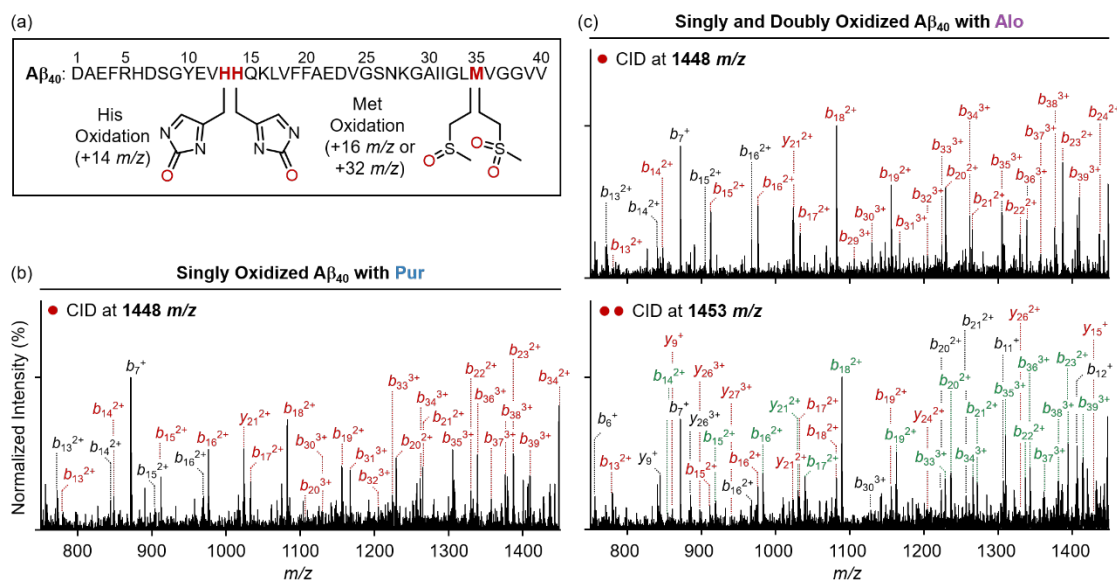
Figure 4. Identification of the oxidized amino acid residues in Aβ₄₀ by the photoactivated **AQ** series through ESI–MS². (a) Sequence of Aβ₄₀ and structures of oxidized His and Met residues. (b and c) ESI–MS² analyses of the singly oxidized peak (m/z = 1448; Figure 3) obtained by treatment of **Pur** as well as the singly and doubly oxidized peaks (m/z = 1448 and 1453, respectively; Figure 3) generated upon incubation with **Alo**. In the ESI–MS² studies, monooxidized and dioxidized b and y ions are illustrated in red and green, respectively. Conditions: [Aβ₄₀] = 25 μM; [compound] = 50 μM; 20 mM ammonium acetate (1% v/v DMSO), pH 7.4; 37 °C; 3 h; constant agitation (250 rpm); Kessil lamp (467 nm) for 1 h. The samples were diluted by 5-fold with H_2O before injection to the mass spectrometer.

doubly, or triply oxidized Aβ₄₀ monomer induced by the light-activated **AQ** series was also noticed in both Zn(II)–Aβ₄₀ and Cu(II)–Aβ₄₀, as shown in Figure S7.

The peaks assigned to oxidized Aβ₄₀ species generated by photoactivation were further probed by ESI–MS² to identify the oxidized amino acid residues (Figure 4a). Aβ₄₀ peptides photooxygenated with **Pur** (**Group A**) and **Alo** (**Group B**) to different extents were selected for tandem MS measurements. Figure 4b exemplifies the collision-induced dissociation (CID) experiments on the singly oxidized peak of Aβ₄₀ (1,448 m/z) obtained by photoexcited **Pur**. We observed b fragments smaller than b_{35} and larger than b_{12} in their nonoxidized and oxidized forms, respectively. The b fragments between b_{13} and b_{34} were found in both nonoxidized and oxidized forms. These observations imply that **Pur** oxidizes either His13, His14, or Met35 separately, but it is unable to simultaneously modify more than one residue. On the contrary, as disclosed in

Figure 4c, ESI–MS^2 studies on the singly and doubly oxidized peaks verified that **Alo** can concurrently oxidize all three aforementioned amino acid residues. The fragmentation analysis on the singly oxidized Aβ$_{40}$ by **Alo** was identical with the results obtained by **Pur**. For the doubly oxidized Aβ$_{40}$, we could not monitor oxidized fragments smaller than b_{13}, and doubly oxidized forms were detected from b ions larger than b_{13}. Note that the Met residue was oxidized up to sulfone in the doubly oxidized Aβ$_{40}$. Overall, our MS studies substantiate that the **AQ** series can oxidize Aβ possibly at the His13, His14, and Met35 residues to varying degrees.

Influence on Aβ Aggregation. To test if the different degree of Aβ oxidation by light activation of the molecules in **Group A** and **Group B** alters the aggregation of both metal-free Aβ and metal–Aβ in a detectable manner, the molecular weight (MW) distribution of the resultant Aβ species was first analyzed by gel electrophoresis with Western blotting (gel/Western blot) using an anti–Aβ antibody (6E10). The morphological change of metal-free Aβ or metal–Aβ aggregates produced by treatment of the **AQ** series was visualized with transmission electron microscopy (TEM). Aβ aggregates larger than ca. 270 kDa are not detectable in gel/Western blot but can be probed by TEM. In this work, we conducted two experiments: (i) inhibition experiments for determining the influence of the **AQ** series on the formation of Aβ aggregates; (ii) disaggregation experiments for assessing the ability of the **AQ** series to disassemble pre-formed Aβ aggregates. In the inhibition experiments, metal-free or metal–Aβ was freshly prepared and treated for 24 h with the **AQ** series, as shown in Figure 5a. For light-exposed samples, Aβ species added with the **AQ** series were photoirradiated for 1 h prior to 24 h incubation. As portrayed in Figure 5b, under dark conditions (grey gels), no significant change in the MW distribution of both metal-free and metal–Aβ$_{40}$ was observed even with the addition of the **AQ** series. Notably, in the presence of light, the resultant Aβ$_{40}$ species with the **AQ** series (blue gels) showed a divergent MW distribution, relative to Aβ$_{40}$ only. Treatment of metal-free Aβ$_{40}$ with light-activated **9,10-AQ**, **HQ**, **Ali**, **Qui**, and **Pur** gave rise to increased signal intensities between ca. 15–35 kDa. Note that the **AQ** series can produce superoxide anion radicals;[61] however, we could not monitor them because the excitation and emission wavelengths used for the assays overlapped with those of the compounds. On the contrary, the illuminated Aβ$_{40}$ samples with **Dan**, **Rhe**, and **Alo** greatly affected the MW distribution exhibiting new gel bands throughout ca. 15–240 kDa. Smearing bands over ca. 240 kDa were spotted for the samples added with both **Group A** and **Group B** indicating that the light-driven oxidation of metal-free Aβ$_{40}$ leads to smaller peptide ensembles that can penetrate the gel matrix. In the inhibition experiments with Zn(II)–Aβ$_{40}$, **9,10-AQ**, **HQ**, **Ali**, **Qui**, and **Pur** upon
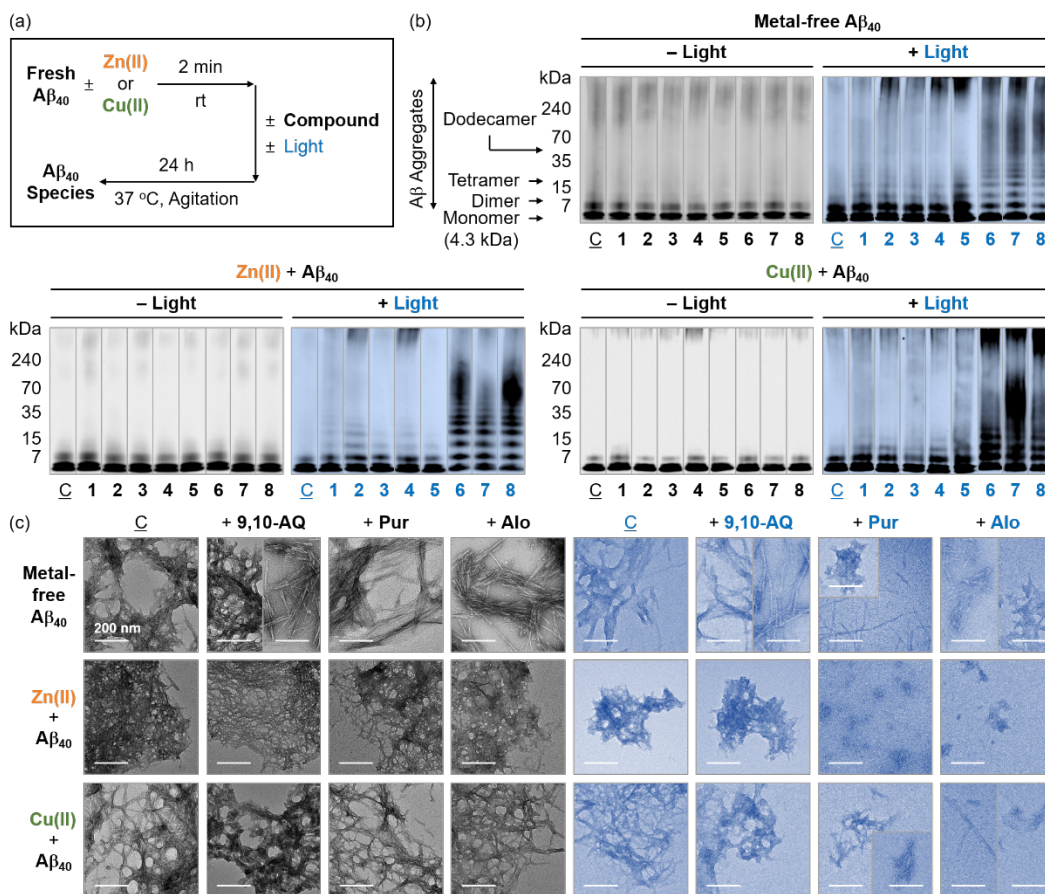
Figure 5. Impact of the **AQ** series on the formation of metal-free or metal-treated Aβ$_{40}$ aggregates with and without light activation. (a) Scheme of the inhibition experiments. (b) Gel/Western blots (anti-Aβ antibody, 6E10) of the resultant Aβ$_{40}$ species upon incubation of metal-free and metal-added Aβ$_{40}$ with and without treatment of compounds and light. Lanes: (C) Aβ$_{40}$; (1) Aβ$_{40}$ + **9,10-AQ**; (2) Aβ$_{40}$ + **HQ**; (3) Aβ$_{40}$ + **Ali**; (4) Aβ$_{40}$ + **Qui**; (5) Aβ$_{40}$ + **Pur**; (6) Aβ$_{40}$ + **Dan**; (7) Aβ$_{40}$ + **Rhe**; (8) Aβ$_{40}$ + **Alo**. (c) TEM images of the aggregates produced upon 24 h incubation of metal-free and metal-treated Aβ$_{40}$ with and without the **AQ** series in the absence and presence of light. Conditions: [Aβ$_{40}$] = 25 μM; [M(II)] = 25 μM; [compound] = 50 μM; 20 mM HEPES (1% v/v DMSO), pH 7.4 [for metal-free or Zn(II)-containing samples] or pH 6.6 [for Cu(II)-added samples], 150 mM NaCl; 37 °C; 24 h; constant agitation (250 rpm); Kessil lamp (467 nm) for 1 h. Scale bar = 200 nm.

photoactivation mildly affected the MW distribution while **Dan**, **Rhe**, and **Alo** significantly enhanced the intensities of the bands between ca. 15–240 kDa. Various aggregates were

detected upon incubation of Cu(II)–Aβ$_{40}$ with photoreactive **Dan**, **Rhe**, and **Alo**, but moderate effects were identified with the illumination of the rest of the **AQ** series.

As described in Figure 5c, metal-free Aβ$_{40}$ and metal–Aβ$_{40}$ aggregates generated with and without the treatment of **9,10-AQ**, **Pur**, or **Alo** were further examined by TEM. **9,10-AQ**, **Pur**, and **Alo** were chosen as the representative molecules of **Parent**, **Group A**, and **Group B**, respectively. Without light, morphologies of the resultant metal–Aβ$_{40}$ aggregates were not significantly changed even with the compounds. Thick fibrils were formed by incubation of metal-free Aβ$_{40}$ in the presence of all three compounds, compared to fibrillary aggregates produced in the sample of metal-free Aβ$_{40}$ only. This suggests that the **AQ** backbone itself may interact with metal-free Aβ$_{40}$ and affect its aggregation. When **9,10-AQ** was incubated with metal-free Aβ$_{40}$ with photoirradiation, long and thick fibrils as well as similar fibrils to those formed from Aβ$_{40}$ only were detected. The conformational transformation of metal-free Aβ$_{40}$ by photoexcited **Pur** and **Alo** was more noticeable than that by **9,10-AQ** resulting in smaller and thinner aggregates. In the case of metal–Aβ$_{40}$ species, small amorphous assemblies and thin fibrils were visualized with the illumination of **Pur** and **Alo**, but **9,10-AQ** did not noticeably alter their morphologies. These amorphous aggregates are reported to be less toxic than structured assemblies.[15,17,19] Modest or no changes found in the structures of metal-free and metal-bound Aβ$_{40}$ species with photoactivated **9,10-AQ** denote the importance of efficient $^1O_2$ production in modifying their aggregation pathways.

Inhibition experiments were also conducted employing Aβ$_{42}$, as presented in Figure S8. The application of light with **9,10-AQ** towards metal-free Aβ$_{42}$ enhanced the band intensity in the high MWs (ca. over 70 kDa). **HQ** and **Ali** did not significantly change MW distribution with photoirradiation. The addition of light-exposed **Qui**, **Pur**, and **Dan** reduced the intensities of the bands in the lower MW region (ca. below 15 kDa) but increased them in the higher MW region (ca. over 70 kDa). This phenomenon was distinct from the samples of **Rhe** and **Alo** with light. In the presence of Zn(II), smearing bands emerged in the case of **Pur**, **Dan**, **Rhe**, and **Alo** throughout ca. 4–270 kDa. In **Ali**- and **Qui**-added samples, a new band at ca. 7 kDa and amplified the intensities of bands over ca. 35 kDa were monitored. Such change of the band above ca. 70 kDa was also observed upon treatment of **9,10-AQ** and **HQ**. The Cu(II)-added samples with the photoilluminated **AQ** series presented the changes in the MW distribution to different extents. Similar to Aβ$_{40}$, TEM studies showed that **9,10-AQ**, **Pur**, and **Alo** did not noticeably alter the morphologies of metal-free and metal–Aβ$_{42}$ aggregates without light. The size of metal-free Aβ$_{42}$ and metal–Aβ$_{42}$ aggregates was greatly diminished by photoexcited **Alo**, and thinner fibrils and smaller aggregates were spotted by addition of **Pur**, compared to compound-free metal-free and metal–Aβ$_{42}$ aggregates.

Moving forwards, as depicted in Figure S9, metal-free or metal–Aβ was pre-incubated for 24 h to form peptide aggregates and the **AQ** series was treated with and without 1 h photoexcitation followed by incubation for an additional 24 h. The gel/Western blots in the disaggregation experiments afforded shifts in the MW distribution of Aβ species to various degrees upon photosensitization of the **AQ** series. Specifically, the MW distribution of pre-formed metal-free Aβ$_{40}$ aggregates was influenced by **9,10-AQ**, **HQ**, **Ali**, **Qui**, **Pur**, **Dan**, and **Rhe** exhibiting new bands between ca. 15–35 kDa. Light-exposed **Ali**, **Qui**, **Pur**, **Dan**, **Rhe**, and **Alo** showed dimmer or no bands in the MW region below ca. 7 kDa. Substantial MW changes of Zn(II)–Aβ$_{40}$ aggregates incubated with **Dan**, **Rhe**, and **Alo** were observed with new bands throughout ca. 15–270 kDa. In the case of **Qui** and **Pur**, the intensities at ca. 7 kDa and above 240 kDa were increased, but photoactivated **9,10-AQ**, **HQ**, and **Ali** manifested less pronounced impact on the MW distribution. The gel/Western blot of pre-formed Cu(II)–Aβ$_{40}$ aggregates also indicated an amplified variation in the MW distribution with **Dan**, **Rhe**, and **Alo** while the treatment of **9,10-AQ** and the molecules in **Group A** resulted in minor or no changes. For metal-free Aβ$_{42}$ aggregates, we were not able to detect a significant MW change with **9,10-AQ**, but slight alterations were found with **HQ** and **Ali**. The addition of **Qui** and **Pur** displayed lower band intensities below ca. 15 kDa. On the other hand, the intensities of the bands throughout the detectable region observed in the sample of Aβ$_{42}$ only were all diminished in the presence of **Dan**, **Rhe**, and **Alo**. Likewise, the MW distribution of metal–Aβ$_{42}$ aggregates with photoactivated **9,10-AQ** was negligibly varied. Against Zn(II)–Aβ$_{42}$ aggregates, the illumination of **Group A** and **Group B** increased the intensity in the higher-order region above ca. 35 kDa. Furthermore, **HQ** and **Qui** produced a new band at ca. 7 kDa with smearing near ca. 15 kDa. **Pur**, **Dan**, **Rhe**, and **Alo** decreased the intensity below ca. 15 kDa. A change in the MW distribution of Cu(II)–Aβ$_{42}$ aggregates was also monitored by treatment of **Group A** and **Group B** in different ranges. Photoactivated **HQ** lowered the intensity between ca. 7–35 kDa, where the bands in the corresponding region became more obscure for **Ali**, **Qui**, and **Pur**. **Dan** resulted in the smearing throughout ca. 7–240 kDa while the bands almost disappeared in the region below ca. 70 kDa for Cu(II)–Aβ$_{42}$ aggregates added with **Rhe** and **Alo**.

Taken together, the gel/Western blot and TEM studies implicitly demonstrate the ability of photoexcited **AQ** series for modulating the formation of metal-free Aβ or metal–Aβ aggregates as well as the disassembly of pre-formed metal-free or metal-added Aβ aggregates. The impact of photoreactive **AQ** series against diverse Aβ species reflects the significance of $^1O_2$ production and the number of oxygen atoms incorporated into Aβ; thus, the compounds in **Group B** are able to remarkably modify the aggregation pathways of both metal-free Aβ and metal–Aβ. Furthermore,

taking account to minimum changes noticed in the parent structure **9,10-AQ**, these in vitro aggregation investigations reveal the relationship between the structural features (e.g., the position and number of hydroxyl groups placed in the framework) of the **AQ** series and the modulatory reactivity towards the aggregation of metal-free Aβ and metal–Aβ.

Biological Efficacies. The cell viability and BBB permeability of the **AQ** series were examined prior to in vivo studies. Photodegradation of photosensitizers during illumination was reported to yield unidentified fragments that can cause toxicity.[62] Thus, the toxicity of the compounds prepared with and without photoirradiation was determined in human neuroblastoma SH-SY5Y (5Y) cells by the MTT assay [MTT = 3-(4,5-dimethylthiazol-2-yl)-2,5-diphenyltetrazolium bromide]. As described in Figure S10, the cells in the presence of both **Group A** and **Group B** without photoactivation exhibited greater survival of over ca. 80% at up to 25 µM. The parent moiety **9,10-AQ** displayed over 70% cell viability. Intriguingly, the toxicity of all molecules pre-illuminated for 1 h before 24 h incubation was lowered by up to ca. 14% at 25 µM. This suggests that the **AQ** series does not yield more toxic products upon photoactivation.

Crossing the BBB is an essential factor for chemical reagents to be utilized in the brain.[63] Thus, the brain uptake of the **AQ** series was predicted by the parallel artificial membrane permeability assay adapted for the BBB.[64,65] As summarized in Table S1, most of the molecules selected in this study were expected to have sufficient BBB penetration with a $-\log P_e$ value below 5.4 except for **Rhe** [$-\log P_e$ of 5.97 (± 0.03)]. The permeability of **9,10-AQ** could not be determined due to limited solubility in water. Moving forward, we chose to examine **Alo** in histochemical investigations in vivo because it showed a relatively high $^1O_2$ quantum yield in the **AQ** series, significant modulatory impact on Aβ aggregation, relatively low cytotoxicity, and potential BBB permeability.

To assess the aggregation propensity of Aβ$_{42}$ species treated with **Alo** and light in the brain, we conducted histochemical studies on the brain samples injected with **Alo**-treated Aβ$_{42}$ species. As illustrated in Figure 6a, Aβ$_{42}$ was freshly prepared in 20 mM HEPES, pH 7.4, 150 mM NaCl (1% v/v DMSO; vehicle), exposed to light for 1 h with and without **Alo**, incubated for an additional 2 h, and directly injected into the hippocampus of murine brains. The hippocampal region is vital for memory formation and retrieval in both murine and human brains and is highly affected by Aβ aggregates formed during the progression of AD.[66-68] After 15 days of injection, the brain sections were obtained and stained with antibodies or fluorescence dyes to determine the deposition of Aβ oligomers or fibrils in the hippocampus. As displayed in Figure 6b, both
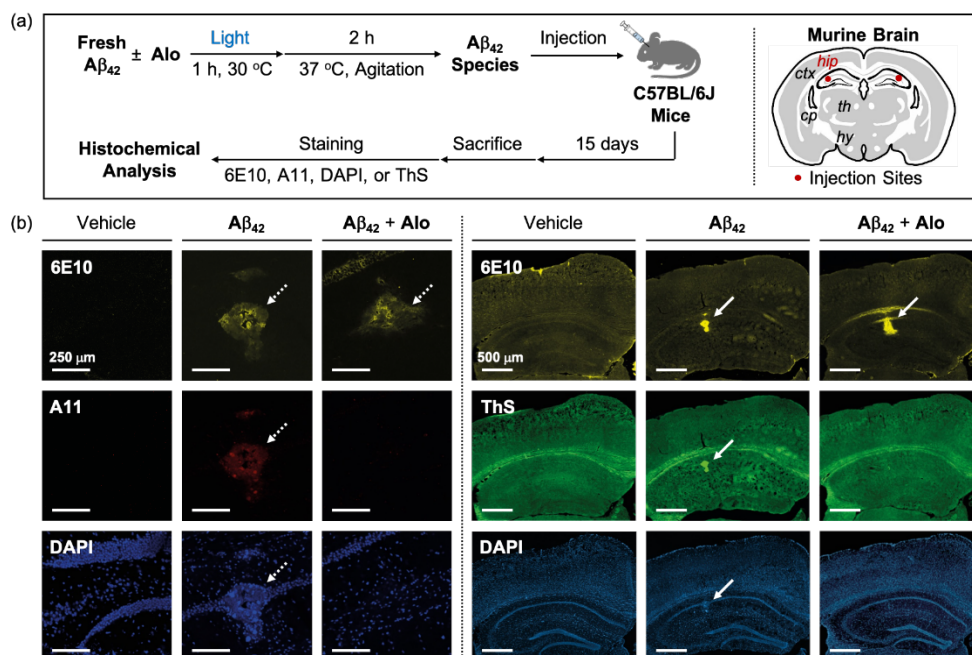
Figure 6. Detection of Aβ$_{42}$ aggregate deposition in murine brains injected with photoactivated **Alo**-treated Aβ$_{42}$ species. (a) Schematic description of histochemical studies and injection sites in the brain. Hippocampus (*hip*), cortex (*ctx*), thalamus (*th*), caudate putamen (*cp*), and hypothalamus (*hy*) are shown. (b) Microscopic images of the hippocampi of C57BL/6J mice injected with vehicle, Aβ$_{42}$, or **Alo**-treated Aβ$_{42}$. Aβ species were prepared in 20 mM HEPES, pH 7.4, 150 mM NaCl (1% v/v DMSO; vehicle) and visualized by immunostaining [primary antibodies, 6E10 (anti-Aβ antibody; yellow) and A11 (anti-oligomer antibody; red), with fluorescent-conjugated secondary antibodies] or fluorescent dyes (ThS for Aβ fibrils; green), and DAPI (for fibrillary Aβ and nucleus; blue). Images were taken by a confocal microscope (left; x10) or a scanning microscope (right; x10). Detected amyloid species are marked with white arrows. Scale bars = 250 μM and 500 μM for confocal or scanning microscopies, respectively. Animal numbers; n = 4 (for Aβ$_{42}$ and **Alo**-added Aβ$_{42}$) and n = 2 (for vehicle).

compound-free and **Alo**-added Aβ$_{42}$ species were safely injected into the hippocampal region, as confirmed by immunostaining with an anti-Aβ primary antibody (6E10).[69,70] Interestingly, only the brain samples, which were administered with compound-free Aβ$_{42}$ species and incubated for a long time in vivo, showed the formation of Aβ$_{42}$ aggregates such as oligomers [detected by immunostaining with an anti-oligomer primary antibody (A11)[71]] or fibrils {visualized with fluorescent dyes [thioflavin-S (ThS) for Aβ fibrils[72,73] or DAPI for Aβ fibrils and cellular nuclei[74,75]]}.

Oligomeric and fibrillar aggregates were not significantly visible in the brain samples injected with Aβ$_{42}$ species oxidized by photoactivated **Alo**. Given that Aβ$_{42}$ oligomers are reported to be neurotoxic by various pathways (e.g., interacting with cellular membranes and damaging intracellular organelles)[13,76,77] and fibrillary amyloid plaques are another pathologic feature upon the progression of AD,[78,79] these overall results imply that the less toxic, off-pathway assembly of the resultant oxidized Aβ species by **Alo** with photoactivation takes place in vivo

CONCLUSIONS

Regulating the aggregation of Aβ peptides via diverse approaches such as chemical transformations has been a long-lasting interest and challenge to alleviate the progression of AD.[13] There has been controversy of the specific role of Aβ in AD, but recent reports continue to emphasize the necessity of our study.[80] The demand of finding an appropriate reagent for PDT oxidatively modifying pathological factors in AD requires both effective $^1O_2$ production and nontoxic byproducts. Our structure-based computational modeling of small **AQ**-based molecules highlights the importance of the adequate level of the singlet-triplet energy gap associated with the reorganization energy throughout the ESIHT process. These conditions were met by incorporating additional hydroxyl groups to form two quasi-ring moieties that facilitate $^1O_2$ production. Spectroscopic and biochemical studies demonstrate the enhanced photoreactivity of the **AQ**-based reagents with two quasi-rings mediated by hydrogen bonding against metal-free Aβ and metal–Aβ, compared to the molecules that possess one or no intramolecular quasi-ring. The **AQ** series also displayed relatively lower cellular toxicity upon photoactivation. Moreover, in the brains of mice, Aβ species generated by **Alo** with light exposure exhibited minimum aggregation into amyloid assemblies such as oligomers or fibrils known to be linked to the pathology of AD. Overall, our combined experimental and computational studies illuminate that the mechanism-based tuning of the intramolecular hydrogen bonds in photosensitizers exhibiting ESIHT leads to prolific outcomes in controlling pathological factors in AD and can contribute towards rationally designing effective chemical reagents for gaining a better understanding of the pathology of the disease.

AUTHOR INFORMATION

Corresponding Author

*miheelim@kaist.ac.kr

*mbaik2805@kaist.ac.kr

*shlee1@kaist.ac.kr

ORCID

Mi Hee Lim: 0000-0003-3377-4996

Mu-Hyun Baik: 0000-0002-8832-8187

Seung-Hee Lee: 0000-0002-9486-5771

Mannkyu Hong: 0000-0002-7770-1230

Author Contributions

ⅡM.H. and M.K. contributed equally to this work.

Notes

The authors declare no competing financial interests.

REFERENCES

(1)   Dolmans, D. E.; Fukumura, D.; Jain, R. K., Photodynamic therapy for cancer. *Nat. Rev. Cancer* **2003**, *3*, 380-387.

(2)   Li, X.; Lovell, J. F.; Yoon, J.; Chen, X., Clinical development and potential of photothermal and photodynamic therapies for cancer. *Nat. Rev. Clin. Oncol.* **2020**, *17*, 657-674.

(3)   Castano, A. P.; Mroz, P.; Hamblin, M. R., Photodynamic therapy and anti-tumour immunity. *Nat. Rev. Cancer* **2006**, *6*, 535-545.

(4)   Huang, H.; Banerjee, S.; Qiu, K.; Zhang, P.; Blacque, O.; Malcomson, T.; Paterson, M. J.; Clarkson, G. J.; Staniforth, M.; Stavros, V. G.; Gasser, G.; Chao, H.; Sadler, P. J., Targeted photoredox catalysis in cancer cells. *Nat. Chem.* **2019**, *11*, 1041-1048.

(5)   Moan, J.; Peng, Q., An outline of the hundred-year history of PDT. *Anticancer Res.* **2003**, *23*, 3591-3600.

(6)   Kessel, D., Photodynamic therapy: from the beginning. *Photodiagnosis Photodyn. Ther.*

2004, *1*, 3-7.

(7)   Baskaran, R.; Lee, J.; Yang, S. G., Clinical development of photodynamic agents and therapeutic applications. *Biomater. Res.* **2018**, *22*, 25.

(8)   Moan, J., Porphyrin photosensitization and phototherapy. *Photochem. Photobiol.* **1986**, *43*, 681-690.

(9)   Gold, M. H.; Goldman, M. P., 5-aminolevulinic acid photodynamic therapy: where we have been and where we are going. *Dermatol. Surg.* **2004**, *30*, 1077-1084.

(10)   Fritsch, C.; Gardlo, K.; Ruzicka, T., Fluorescence diagnosis in dermatology. In *Dermatological phototherapy and photodiagnostic methods*, Springer: Berlin, Heidelberg, 2009; pp 387-414.

(11)   Alvarado, D. R.; Argyropoulos, D. S.; Scholle, F.; Peddinti, B. S. T.; Ghiladi, R. A., A facile strategy for photoactive nanocellulose-based antimicrobial materials. *Green Chem.* **2019**, *21*, 3424-3435.

(12)   Peddinti, B. S. T.; Morales-Gagnon, N.; Pourdeyhimi, B.; Scholle, F.; Spontak, R. J.; Ghiladi, R. A., Photodynamic coatings on polymer microfibers for pathogen inactivation: Effects of application method and composition. *ACS Appl. Mater. Interfaces* **2021**, *13*, 155-163.

(13)   Savelieff, M. G.; Nam, G.; Kang, J.; Lee, H. J.; Lee, M.; Lim, M. H., Development of multifunctional molecules as potential therapeutic candidates for Alzheimer's disease, Parkinson's disease, and amyotrophic lateral sclerosis in the last decade. *Chem. Rev.* **2019**, *119*, 1221-1322.

(14)   Li, C.; Wang, J.; Liu, L., Alzheimer's therapeutic strategy: photoactive platforms for suppressing the aggregation of amyloid β protein. *Front. Chem.* **2020**, *8*, 1-6.

(15)   Kim, M.; Kang, J.; Lee, M.; Han, J.; Nam, G.; Tak, E.; Kim, M. S.; Lee, H. J.; Nam, E.; Park, J.; Oh, S. J.; Lee, J. Y.; Lee, J. Y.; Baik, M. H.; Lim, M. H., Minimalistic principles for designing small molecules with multiple reactivities against pathological factors in dementia. *J. Am. Chem. Soc.* **2020**, *142*, 8183-8193.

(16)   Nam, E.; Derrick, J. S.; Lee, S.; Kang, J.; Han, J.; Lee, S. J. C.; Chung, S. W.; Lim, M. H., Regulatory activities of dopamine and its derivatives toward metal-free and metal-induced amyloid-β aggregation, oxidative stress, and inflammation in Alzheimer's disease. *ACS Chem. Neurosci.* **2018**, *9*, 2655-2666.

(17)   Beck, M. W.; Derrick, J. S.; Kerr, R. A.; Oh, S. B.; Cho, W. J.; Lee, S. J.; Ji, Y.; Han, J.; Tehrani, Z. A.; Suh, N.; Kim, S.; Larsen, S. D.; Kim, K. S.; Lee, J. Y.; Ruotolo, B. T.; Lim, M. H., Structure-mechanism-based engineering of chemical regulators targeting distinct pathological factors in Alzheimer's disease. *Nat. Commun.* **2016**, *7*, 13115.

(18) Beck, M. W.; Derrick, J. S.; Suh, J. M.; Kim, M.; Korshavn, K. J.; Kerr, R. A.; Cho, W. J.; Larsen, S. D.; Ruotolo, B. T.; Ramamoorthy, A.; Lim, M. H., Minor structural variations of small molecules tune regulatory activities toward pathological factors in Alzheimer's disease. *ChemMedChem* **2017**, *12*, 1828-1838.

(19) Derrick, J. S.; Kerr, R. A.; Nam, Y.; Oh, S. B.; Lee, H. J.; Earnest, K. G.; Suh, N.; Peck, K. L.; Ozbil, M.; Korshavn, K. J.; Ramamoorthy, A.; Prabhakar, R.; Merino, E. J.; Shearer, J.; Lee, J. Y.; Ruotolo, B. T.; Lim, M. H., A redox-active, compact molecule for cross-linking amyloidogenic peptides into nontoxic, off-pathway aggregates: in vitro and in vivo efficacy and molecular mechanisms. *J. Am. Chem. Soc.* **2015**, *137*, 14785-14797.

(20) Han, J.; Lee, H. J.; Kim, K. Y.; Lee, S. J. C.; Suh, J. M.; Cho, J.; Chae, J.; Lim, M. H., Tuning structures and properties for developing novel chemical tools toward distinct pathogenic elements in Alzheimer's disease. *ACS Chem. Neurosci.* **2018**, *9*, 800-808.

(21) Ishida, Y.; Tanimoto, S.; Takahashi, D.; Toshima, K., Photo-degradation of amyloid β by a designed fullerene–sugar hybrid. *Med. Chem. Commun.* **2010**, *1*, 212-215.

(22) Lee, B. I.; Lee, S.; Suh, Y. S.; Lee, J. S.; Kim, A. K.; Kwon, O. Y.; Yu, K.; Park, C. B., Photoexcited porphyrins as a strong suppressor of β-amyloid aggregation and synaptic toxicity. *Angew. Chem. Int. Ed.* **2015**, *54*, 11472-11476.

(23) Kang, J.; Lee, S. J.; Nam, J. S.; Lee, H. J.; Kang, M. G.; Korshavn, K. J.; Kim, H. T.; Cho, J.; Ramamoorthy, A.; Rhee, H. W.; Kwon, T. H.; Lim, M. H., An iridium(III) complex as a photoactivatable tool for oxidation of amyloidogenic peptides with subsequent modulation of peptide aggregation. *Chem. Eur. -J.* **2017**, *23*, 1645-1653.

(24) Leung, C. H.; Zhong, H. J.; Chan, D. S. H.; Ma, D. L., Bioactive iridium and rhodium complexes as therapeutic agents. *Coord. Chem. Rev.* **2013**, *257*, 1764-1776.

(25) Man, B. Y.-W.; Chan, H.-M.; Leung, C.-H.; Chan, D. S.-H.; Bai, L.-P.; Jiang, Z.-H.; Li, H.-W.; Ma, D.-L., Group 9 metal-based inhibitors of β-amyloid (1–40) fibrillation as potential therapeutic agents for Alzheimer's disease. *Chem. Sci.* **2011**, *2*, 917-921.

(26) Wong, C. Y.; Chung, L. H.; Lu, L. H.; Wang, M.; He, B. Y.; Liu, L. J.; Leung, C. H.; Ma, D.-L., Dual inhibition and monitoring of beta-amyloid fibrillation by a luminescent iridium(III) complex. *Curr. Alzheimer Res.* **2015**, *12*, 439-444.

(27) Gomes, L. M. F.; Bataglioli, J. C.; Storr, T., Metal complexes that bind to the amyloid-β peptide of relevance to Alzheimer's disease. *Coord. Chem. Rev.* **2020**, *412*, 213255.

(28) Bataglioli, J. C.; Gomes, L. M. F.; Maunoir, C.; Smith, J. R.; Cole, H. D.; McCain, J.; Sainuddin, T.; Cameron, C. G.; McFarland, S. A.; Storr, T., Modification of amyloid-beta peptide aggregation via photoactivation of strained Ru(II) polypyridyl complexes. *Chem. Sci.*

2021, *12*, 7510-7520.

(29) Chung, Y. J.; Lee, C. H.; Lim, J.; Jang, J.; Kang, H.; Park, C. B., Photomodulating carbon dots for spatiotemporal suppression of Alzheimer's β-amyloid aggregation. *ACS Nano* **2020**, *14*, 16973-16983.

(30) Kim, K.; Lee, S. H.; Choi, D. S.; Park, C. B., Photoactive bismuth vanadate structure for light-triggered dissociation of Alzheimer's β-amyloid aggregates. *Adv. Funct. Mater.* **2018**, *28*, 1802813.

(31) Lee, J. S.; Lee, B. I.; Park, C. B., Photo-induced inhibition of Alzheimer's β-amyloid aggregation in vitro by rose bengal. *Biomaterials* **2015**, *38*, 43-49.

(32) Taniguchi, A.; Sasaki, D.; Shiohara, A.; Iwatsubo, T.; Tomita, T.; Sohma, Y.; Kanai, M., Attenuation of the aggregation and neurotoxicity of amyloid-β peptides by catalytic photooxygenation. *Angew. Chem. Int. Ed.* **2014**, *53*, 1382-1385.

(33) Ni, J.; Taniguchi, A.; Ozawa, S.; Hori, Y.; Kuninobu, Y.; Saito, T.; Saido, T. C.; Tomita, T.; Sohma, Y.; Kanai, M., Near-infrared photoactivatable oxygenation catalysts of amyloid peptide. *Chem* **2018**, *4*, 807-820.

(34) Lee, B. I.; Suh, Y. S.; Chung, Y. J.; Yu, K.; Park, C. B., Shedding light on Alzheimer's β-amyloidosis: photosensitized methylene blue inhibits self-assembly of β-amyloid peptides and disintegrates their aggregates. *Sci. Rep.* **2017**, *7*, 7523.

(35) Pardridge, W. M., Drug transport across the blood-brain barrier. *J. Cereb. Blood Flow Metab.* **2012**, *32*, 1959-1972.

(36) Zheng, W.; Aschner, M.; Ghersi-Egea, J. F., Brain barrier systems: a new frontier in metal neurotoxicological research. *Toxicol. Appl. Pharmacol.* **2003**, *192*, 1-11.

(37) Egorova, K. S.; Ananikov, V. P., Toxicity of metal compounds: knowledge and myths. *Organometallics* **2017**, *36*, 4071-4090.

(38) Win-Shwe, T. T.; Fujimaki, H., Nanoparticles and neurotoxicity. *Int. J. Mol. Sci.* **2011**, *12*, 6267-6280.

(39) Vutskits, L.; Briner, A.; Klauser, P.; Gascon, E.; Dayer, A. G.; Kiss, J. Z.; Muller, D.; Licker, M. J.; Morel, D. R., Adverse effects of methylene blue on the central nervous system. *Anesthesiology* **2008**, *108*, 684-692.

(40) Frank, M.; Ahrens, J.; Bejenke, I.; Krick, M.; Schwarzer, D.; Clever, G. H., Light-induced charge separation in densely packed donor-acceptor coordination cages. *J. Am. Chem. Soc.* **2016**, *138*, 8279-8287.

(41) Lee, W.; Jung, S.; Kim, M.; Hong, S., Site-selective direct C–H pyridylation of unactivated alkanes by triplet excited anthraquinone. *J. Am. Chem. Soc.* **2021**, *143*, 3003-3012.

21

(42) Kawaai, K.; Yamaguchi, T.; Yamaguchi, E.; Endo, S.; Tada, N.; Ikari, A.; Itoh, A., Photoinduced generation of acyl radicals from simple aldehydes: access to 3-acyl-4-arylcoumarin derivatives, and evaluation of their antiandrogenic activities. *J. Org. Chem.* **2018**, *83*, 1988-1996.

(43) Yadav, R. K.; Baeg, J. O.; Oh, G. H.; Park, N. J.; Kong, K. J.; Kim, J.; Hwang, D. W.; Biswas, S. K., A photocatalyst-enzyme coupled artificial photosynthesis system for solar energy in production of formic acid from CO_2. *J. Am. Chem. Soc.* **2012**, *134*, 11455-11461.

(44) Reece, S. Y.; Seyedsayamdost, M. R.; Stubbe, J.; Nocera, D. G., Photoactive peptides for light-initiated tyrosyl radical generation and transport into ribonucleotide reductase. *J. Am. Chem. Soc.* **2007**, *129*, 8500-8509.

(45) Ou, H. D.; Phan, S.; Deerinck, T. J.; Thor, A.; Ellisman, M. H.; O'Shea, C. C., ChromEMT: Visualizing 3D chromatin structure and compaction in interphase and mitotic cells. *Science* **2017**, *357*, eaag0025.

(46) Chen, G. F.; Xu, T. H.; Yan, Y.; Zhou, Y. R.; Jiang, Y.; Melcher, K.; Xu, H. E., Amyloid beta: structure, biology and structure-based therapeutic development. *Acta. Pharmacol. Sin.* **2017**, *38*, 1205-1235.

(47) Montoya, S. C.; Comini, L. R.; Sarmiento, M.; Becerra, C.; Albesa, I.; Arguello, G. A.; Cabrera, J. L., Natural anthraquinones probed as Type I and Type II photosensitizers: singlet oxygen and superoxide anion production. *J. Photochem. Photobiol. B* **2005**, *78*, 77-83.

(48) Gollnick, K.; Held, S.; Martire, D. O.; Braslavsky, S. E., Hydroxyanthraquinones as sensitizers of singlet oxygen reactions - quantum yields of triplet formation and singlet oxygen generation in acetonitrile. *J. Photochem. Photobiol. A* **1992**, *69*, 155-165.

(49) Bredas, J. L.; Beljonne, D.; Coropceanu, V.; Cornil, J., Charge-transfer and energy-transfer processes in p-conjugated oligomers and polymers: a molecular picture. *Chem. Rev.* **2004**, *104*, 4971-5004.

(50) Mohammed, O. F.; Xiao, D.; Batista, V. S.; Nibbering, E. T., Excited-state intramolecular hydrogen transfer (ESIHT) of 1,8-dihydroxy-9,10-anthraquinone (DHAQ) characterized by ultrafast electronic and vibrational spectroscopy and computational modeling. *J. Phys. Chem. A* **2014**, *118*, 3090-3099.

(51) Flom, S. R.; Barbara, P. F., Proton transfer and hydrogen bonding in the internal conversion of S1 anthraquinones. *J. Phys. Chem.* **2002**, *89*, 4489-4494.

(52) Choi, J. R.; Jeoung, S. C.; Cho, D. W., Time-resolved anisotropy study on the excited-state intramolecular proton transfer of 1-hydroxyanthraquinone. *Bull. Korean Chem. Soc.* **2003**, *24*, 1675-1679.

(53) Suess, C. J.; Hirst, J. D.; Besley, N. A., Quantum chemical calculations of tryptophan -> heme electron and excitation energy transfer rates in myoglobin. *J. Comput. Chem.* **2017**, *38*, 1495-1502.

(54) Subotnik, J. E.; Vura-Weis, J.; Sodt, A. J.; Ratner, M. A., Predicting accurate electronic excitation transfer rates via marcus theory with Boys or Edmiston-Ruedenberg localized diabatization. *J. Phys. Chem. A* **2010**, *114*, 8665-8675.

(55) Sherbrook, E. M.; Jung, H. M.; Cho, D.; Baik, M. H.; Yoon, T. P., Bronsted acid catalysis of photosensitized cycloadditions. *Chem. Sci.* **2020**, *11*, 856-861.

(56) Miliani, C.; Romani, A.; Favaro, G., Acidichromic effects in 1,2-di- and 1,2,4-tri-hydroxyanthraquinones. A spectrophotometric and fluorimetric study. *J. Phys. Org. Chem.* **2000**, *13*, 141-150.

(57) Pareras, G.; Palusiak, M.; Duran, M.; Sola, M.; Simon, S., Tuning the strength of the resonance-assisted hydrogen bond in *o*-hydroxybenzaldehyde by substitution in the aromatic ring. *J. Phys. Chem. A* **2018**, *122*, 2279-2287.

(58) Suzuki, K.; Kobayashi, A.; Kaneko, S.; Takehira, K.; Yoshihara, T.; Ishida, H.; Shiina, Y.; Oishi, S.; Tobita, S., Reevaluation of absolute luminescence quantum yields of standard solutions using a spectrometer with an integrating sphere and a back-thinned CCD detector. *Phys. Chem. Chem. Phys.* **2009**, *11*, 9850-9860.

(59) Wessels, J. M.; Foote, C. S.; Ford, W. E.; Rodgers, M. A., Photooxidation of tryptophan: $O_2(^1\Delta_g)$ versus electron-transfer pathway. *Photochem. Photobiol.* **1997**, *65*, 96-102.

(60) Nam, J. S.; Kang, M. G.; Kang, J.; Park, S. Y.; Lee, S. J.; Kim, H. T.; Seo, J. K.; Kwon, O. H.; Lim, M. H.; Rhee, H. W.; Kwon, T. H., Endoplasmic reticulum-localized iridium(III) complexes as efficient photodynamic therapy agents via protein modifications. *J. Am. Chem. Soc.* **2016**, *138*, 10968-10977.

(61) Latour, V.; Pigot, T.; Simon, M.; Cardy, H.; Lacombe, S., Photo-oxidation of di-n-butylsulfide by various electron transfer sensitizers in oxygenated acetonitrile. *Photochem. Photobiol. Sci.* **2005**, *4*, 221-229.

(62) Dhakal, P.; Kuzyk, M. G., Molecular structure and reversible photodegradation in anthraquinone dyes. *J. Photochem. Photobiol. A* **2016**, *328*, 66-76.

(63) Ni, W.; Chen, W.; Lu, Y., Emerging findings into molecular mechanism of brain metastasis. *Cancer Med.* **2018**, *7*, 3820-3833.

(64) Avdeef, A.; Bendels, S.; Di, L.; Faller, B.; Kansy, M.; Sugano, K.; Yamauchi, Y., PAMPA-critical factors for better predictions of absorption. *J. Pharm. Sci.* **2007**, *96*, 2893-2909.

(65) Di, L.; Kerns, E. H.; Fan, K.; McConnell, O. J.; Carter, G. T., High throughput artificial

membrane permeability assay for blood-brain barrier. *Eur. J. Med. Chem.* **2003**, *38*, 223-232.

(66) Mormino, E. C.; Kluth, J. T.; Madison, C. M.; Rabinovici, G. D.; Baker, S. L.; Miller, B. L.; Koeppe, R. A.; Mathis, C. A.; Weiner, M. W.; Jagust, W. J., Episodic memory loss is related to hippocampal-mediated beta-amyloid deposition in elderly subjects. *Brain* **2009**, *132*, 1310-1323.

(67) Reilly, J. F.; Games, D.; Rydel, R. E.; Freedman, S.; Schenk, D.; Young, W. G.; Morrison, J. H.; Bloom, F. E., Amyloid deposition in the hippocampus and entorhinal cortex: quantitative analysis of a transgenic mouse model. *Proc. Natl. Acad. Sci. U. S. A.* **2003**, *100*, 4837-4842.

(68) Wengenack, T. M.; Whelan, S.; Curran, G. L.; Duff, K. E.; Poduslo, J. F., Quantitative histological analysis of amyloid deposition in Alzheimer's double transgenic mouse brain. *Neuroscience* **2000**, *101*, 939-944.

(69) Kim, K. S.; Miller, D. L.; Sapienza, V. J.; Chen, C. M. J.; Bai, C.; Grundke-Iqbal, I.; Currie, C. J.; Wisniewski, H. M., Production and characterization of monoclonal antibodies reactive to synthetic cerebrovascular amyloid peptide. *Neurosci. Res. Commun.* **1988**, *2*, 121-130.

(70) Kim, K. S.; Wen, G. Y.; Bancher, C.; Chen, C. M. J.; Sapienza, V. J.; Hong, H.; Wisniewski, H. M., Detection and quantitation of amyloid beta-peptide with 2 monoclonal antibodies. *Neurosci. Res. Commun.* **1990**, *7*, 113-122.

(71) Kayed, R.; Head, E.; Thompson, J. L.; McIntire, T. M.; Milton, S. C.; Cotman, C. W.; Glabe, C. G., Common structure of soluble amyloid oligomers implies common mechanism of pathogenesis. *Science* **2003**, *300*, 486-489.

(72) Kelenyi, G., Thioflavin S fluorescent and Congo red anisotropic stainings in the histologic demonstration of amyloid. *Acta Neuropathol.* **1967**, *7*, 336-348.

(73) Urbanc, B.; Cruz, L.; Le, R.; Sanders, J.; Ashe, K. H.; Duff, K.; Stanley, H. E.; Irizarry, M. C.; Hyman, B. T., Neurotoxic effects of Thioflavin S-positive amyloid deposits in transgenic mice and Alzheimer's disease. *Proc. Natl. Acad. Sci. U. S. A.* **2002**, *99*, 13990-13995.

(74) Mora, A. K.; Khan, S.; Patro, B. S.; Nath, S., Is DAPI assay of cellular nucleic acid reliable in the presence of protein aggregates? *Chem. Commun.* **2020**, *56*, 13844-13847.

(75) Simard, A. R.; Soulet, D.; Gowing, G.; Julien, J. P.; Rivest, S., Bone marrow-derived microglia play a critical role in restricting senile plaque formation in Alzheimer's disease. *Neuron* **2006**, *49*, 489-502.

(76) Lee, S. J.; Nam, E.; Lee, H. J.; Savelieff, M. G.; Lim, M. H., Towards an understanding of amyloid-beta oligomers: characterization, toxicity mechanisms, and inhibitors. *Chem. Soc. Rev.* **2017**, *46*, 310-323.

(77) Benilova, I.; Karran, E.; De Strooper, B., The toxic Abeta oligomer and Alzheimer's disease: an emperor in need of clothes. *Nat. Neurosci.* **2012**, *15*, 349-357.

(78) Lorenzo, A.; Yankner, B. A., Amyloid fibril toxicity in Alzheimer's disease and diabetes. *Ann. N. Y. Acad. Sci.* **1996**, *777*, 89-95.

(79) Tsai, J.; Grutzendler, J.; Duff, K.; Gan, W. B., Fibrillar amyloid deposition leads to local synaptic abnormalities and breakage of neuronal branches. *Nat. Neurosci.* **2004**, *7*, 1181-1183.

(80) Chen, W. T.; Lu, A.; Craessaerts, K.; Pavie, B.; Sala Frigerio, C.; Corthout, N.; Qian, X.; Lalakova, J.; Kuhnemund, M.; Voytyuk, I.; Wolfs, L.; Mancuso, R.; Salta, E.; Balusu, S.; Snellinx, A.; Munck, S.; Jurek, A.; Fernandez Navarro, J.; Saido, T. C.; Huitinga, I.; Lundeberg, J.; Fiers, M.; De Strooper, B., Spatial transcriptomics and in situ sequencing to study Alzheimer's disease. *Cell* **2020**, *182*, 976-991.